Performance of Mechanisms and Reactor Models for Methane Oxidation on Rh

Kenneth A. Williams, Raimund Horn, and Lanny D. Schmidt
Dept. of Chemical Engineering and Materials Science, University of Minnesota, Minneapolis, MN 55455

DOI 10.1002/aic.11244
Published online July 2, 2007 in Wiley InterScience (www.interscience.wiley.com).

Numerical simulations of methane catalytic partial oxidation on Rh-coated foam monoliths were performed and tested against high-resolution species and temperature profiles measured along the catalyst axis. A systematic comparison considering 2D models with heat and mass transport and a 1D reactor model with two multistep surface chemistry mechanisms is presented for feed conditions of 5 standard liters per minute, atmospheric pressure, and C/O *ratios of 0.7, 1.0, and 1.3. Agreement between experimental data and the plug flow model and is for all conditions inferior to agreement with 2D models. 2D simulation profiles and the measured profiles agree qualitatively for all experimental conditions. Quantitative agreement is best for syngas stoichiometry* (C/O = *1.0), while some differences are observed for* C/O = *0.7 and 1.3.* H_2 *and CO production in the presence of* O_2 *is found to be strongly dependent on catalyst temperature. Accordingly, the importance of high-resolution spatial profiles for mechanism and reactor model validation is highlighted.* © 2007 American Institute of Chemical Engineers *AIChE J,* 53: 2097–2113, 2007

Keywords: catalytic partial oxidation, methane, rhodium, numerical simulation, surface mechanism

Introduction

Methane conversion into hydrogen, liquid fuels, and chemicals is of growing economic importance since oil production may peak before year 2040 according to recent assessments.[1] Strong efforts in science and technology are underway to convert natural gas into liquids to open up an alternative petroleum resource that can compensate potential oil shortfalls.[2] Production of syngas is the first step in the conversion of methane to liquids. Methane catalytic partial oxidation (CPO) on Rh-coated foam monoliths is an efficient way to achieve this transformation.[3] The CPO reaction (Eq. 1) is slightly exothermic in contrast to highly endothermic steam reforming (Eq. 2):

$$CH_4 + \frac{1}{2}\,O_2 \rightarrow CO + 2H_2 \quad \Delta H_R^o = -35.6 \text{ kJ/mol } CH_4 \quad (1)$$

$$CH_4 + H_2O \rightarrow CO + 3H_2 \quad \Delta H_R^o = +206 \text{ kJ/mol } CH_4 \quad (2)$$

Steam reforming on Ni requires contact times in the range of 1 s to achieve sufficient methane conversion. Autothermal millisecond CPO reactors holds great promise for replacing steam reformers and steam crackers for production of hydrogen and olefins, respectively, because they operate at much shorter residence times, require much simpler equipment, and can be scaled up or down for different applications.[2,4–6] For CPO on Rh, CH_4 conversion close to 100% and >90% selectivities to H_2 and CO can be achieved in a few ms.[4] For process integration, methane CPO supplies a H_2/CO ratio of 2 that is more favorable for downstream chemistry (methanol, Fischer-Tropsch synthesis) than the higher ratio of 3 obtained by steam reforming.

Correspondence concerning this article should be addressed to L. D. Schmidt at schmi001@umn.edu.
Current address of Kenneth A. Williams: Cargill, Inc., Process Solutions Technology Development Center, Crescent Ridge II, 10900 Wayzata Blvd., Suite 2-164, Minnetonka, MN 55305.

In spite of several decades of research on millisecond reactors, many questions remain concerning the mechanism of the process. A major challenge is that the process cannot be decomposed into simple laboratory experiments from which kinetics and catalysts can be examined systematically. This is because realistic temperature and concentration profiles cannot be created without the presence of interphase mass and heat transfer that may change the process significantly. Temperatures above $\sim 800^{\circ}C$ are required to prevent total oxidation and significant carbon formation within the catalyst. Large gradients in temperature ($>10^5$ K/s) and concentration are necessary to prevent combustion before the catalyst and to quench primary products after the catalyst. There is an ongoing debate about the mechanism of methane CPO. Direct and indirect mechanisms have been postulated, discussed, and reviewed in the literature.[7] A brief summary of key experimental observations regarding CPO on Rh can be found elsewhere.[8]

Reactor models and multi-step chemistry

Detailed modeling with plug flow reactor (PFR) and two-dimensional (2D) simulations has been used to simulate methane oxidation to syngas[9–13] and ethane oxidation to ethylene[14–16] over Rh and Pt catalysts using up to 100 steps for surface reactions and hundreds of steps for gas-phase reactions. However, while these simulations predict conversions and selectivities accurately, for the most part only experimental exit compositions (integral data) were used for validating the postulated mechanisms because little information has been available regarding species compositions within the catalyst. As with experimental studies, previous numerical studies differ in their conclusions about the reaction mechanism.

Early work on methane oxidation over noble metals assumed a direct mechanism because a high temperature surface model (19 reactions) was developed that agreed with experimental integral conversion and selectivity data reasonably well.[9,17] In this surface scheme, CH_4 dissociation on metallic Rh sites was lumped into a single step, and H_2 and CO were formed as primary products. Except for CO_2 adsorption, all adsorption–desorption steps in this original surface mechanism were reversible. Steam reforming was not excluded by definition, but CO_2 reforming was (low sticking coefficient of CO_2 on Rh). 2D simulations using this mechanism showed no steam reforming contribution;[10] it was too slow given the kinetic parameters used. A PFR study[11] using the 19-step surface model and large gas-phase mechanisms[18,19] showed that gas-phase reactions were insignificant at atmospheric pressure for millisecond contact times but become important at elevated pressures (>5 bar).[10,20] Experimental results corroborate these findings.[21]

The mechanism was further extended to 38 reversible reactions by including steam reforming, water-gas-shift (WGS), and CO_2 readsorption.[22] These refinements are in better agreement with experiments showing that steam reforming on Rh is possible at millisecond contact times.[22–24] The 38-step surface mechanism has been validated against integral steady-state[12,25] and transient experimental data.[13,26] Coverage-dependent desorption energies for CO and O_2 were included[13] for better lightoff agreement.

More recently, a 104-step C_1 mechanism on Rh was reported by Mhadeshwar and Vlachos, which was partially derived from first-principles simulation.[27] All activation energies in this mechanism were either coverage or temperature dependent or both. Besides methane CPO, this mechanism also considered methane reforming by water and CO_2 and decomposition of oxygenates on Rh. According to the authors, this mechanism predicts distinct oxidation (CO_2 and H_2O as products) and reforming (CO and H_2 as products) zones for methane CPO. H_2 formation was not found in the presence of gas-phase oxygen for experiments closely matching the present work based on the temperature profiles used in their simulations.

Previous experimental/numerical spatial profile comparisons

Numerous studies have been performed to determine axial temperatures (gas and surface) within working catalysts; however, high-resolution differential composition profiles were lacking until recently.[8,28] Temperatures have been measured in extruded monoliths, fixed beds, or gauzes with IR thermography and thermocouples,[29–33] but these experiments may introduce radiation and conduction losses compared to insulated catalysts. One-dimensional multi-phase (heterogeneous) simulations of a fixed bed coupling surface chemistry with interphase transport and external heat loss show that experimentally measured gas and surface temperatures can be quantitatively reproduced.[25] Axial species profiles have been approximated by measuring exit compositions using different catalyst lengths with different thickness monoliths[23] or with sphere beds of different lengths,[34] but these do not necessarily duplicate the profiles within a single foam catalyst. Axial fuel conversion profiles were measured for natural gas on Pt-coated honeycomb monoliths and simulated using detailed heterogeneous surface chemistry.[35] Species concentration profiles for methane oxidation on Rh at high pressure have been measured by gas chromatography sampling between multiple metal catalyst screen layers.[36] PFR simulations with C_1 chemistry on Rh[27] were compared to the axial measured profiles[36] with the conclusion that CO and H_2O were the primary oxidation products in presence of gas phase O_2, whereas H_2 was a secondary product formed by steam reforming after complete conversion of gas phase O_2.

High-resolution spatial profile measurements have been used to validate heterogeneous and homogeneous mechanisms for methane oxidation in stagnation flow and catalytic channel reactors. A stagnation flow reactor (planar catalyst) with a quartz microprobe and mass spectrometer was used to study the catalytic combustion of methane at atmospheric pressure on a hexaaluminate catalyst[37,38] and estimate global surface reaction rates. Raman and laser-induced fluorescence measurements over the catalyst boundary layer in a laminar channel flow reactor have been performed from 1 to 16 bar;[39,40] these measurements were used to test the performance of state-of-the-art surface and gas phase chemistry mechanisms at high pressure. Additionally, axial variation of the oxidation state for a Pt/Rh catalyst[41] and axial/radial vari-

ation of the oxidation state for a Rh catalyst[42] were measured for methane CPO using X-ray absorption spectroscopy.

Motivation

From these studies, it is clear that high-resolution spatially-resolved experimental data are needed to discriminate between a number of multi-step surface mechanisms and reactor models that predict integral data equally well. An experimental method has been developed to measure axial species and temperature profiles within CPO foam monoliths at atmospheric pressure with 0.3-mm spatial resolution using a capillary sampling technique with a mass spectrometer.[8,28,43] 2D simulations with a 38-step mechanism[12] were found to fit experimental profiles well at $C/O = 1.0$, but some deficiencies were found at $C/O = 0.7$ and 1.3 (Ref. 8).

The goal of this work is the systematic performance analysis of two state-of-the-art surface mechanisms for methane CPO in comparison to high-resolution axial data measured in an adiabatically operated reactor with a Rh-coated ceramic foam. All experimental data shown in this work have been measured with the capillary sampling technique described in previous work,[28,43] where experimental details can be found. The two mechanisms used are a 38-step surface reaction mechanism with[13]/without[12] coverage dependencies and a 104-step mechanism with full coverage dependence.[27] Strengths and weaknesses of both mechanisms are discussed over a range of feed stoichiometries ($C/O = 0.7$, 1.0, and 1.3). In addition, the role of the reactor models (1D and 2D) and gas and surface temperatures on model predictions are explored with the 38-step mechanism.

Numerical Methods

PFR model

In one embodiment of the reacting system, a single cylindrical hypothetical pore of a 10-mm long 80-ppi foam monolith was simulated using a PFR model and a nominal pore diameter of 0.25 mm (area/volume = 160 cm^{-1}), effectively neglecting the tortuous pore network present in ceramic foams. The differential algebric equations resulting from the plug-flow treatment were solved using Chemkin PLUG[44,45] or Detchem Plug[46] code.

2D pore channel model

In a second embodiment of the system, the single hypothetical pore of the 10-mm long 80 ppi foam was simulated using computational fluid dynamics (CFD) in a 2D axisymmetric and elliptic PDE treatment solving the applicable transport equations for both solid and gas phases. This model is similar to that previously used to model ethane oxidative dehydrogenation (see Figure 1 of that work).[15] The catalyst channel is 10-mm long as are the front and back heat shield channels. Channel diameter is 0.25 mm, while the wall thickness is 0.055 mm. Solid phase was modeled using the thermal properties of alumina as a polynomial function of temperature (thermal conductivity varies from 36 to 5 W/(m K) from 300 to 1500 K).[47,48] Solution procedures were the same as described in the next section.

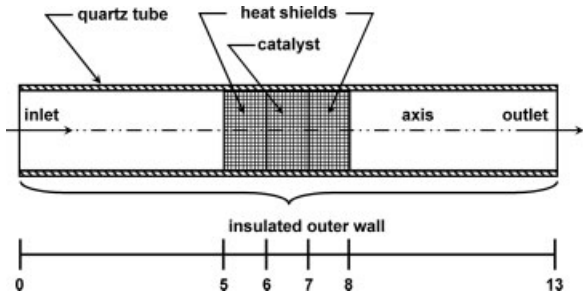

Figure 1. Schematic of computational domain for the 2D porous media model.

Only the top half of the domain shown is simulated because of axisymmetry. The heat shields and catalyst (crosshatched regions) are modeled using a 1D sub-grid treatment that accounts for the effect of the porous media on flow and transport. Horizontal scale units are cm.

2D porous media model

The final embodiment of the reacting system consists of a 2D axisymmetric porous model to simulate reactor conditions and intra-construct species profiles using CFD; a treatment similar to a sub-grid scale model used previously to model catalytic converter chemistry.[49] This model incorporated the entire reactor geometry and dimensions. Because of radial symmetry, only one half of the axial cross-section of the reactor tube was considered.

A schematic of the computational grid is shown in Figure 1. The grid is comprised of the fluid zone (inner diameter = 19 mm) and the reactor wall (quartz tube, outer diameter = 22 mm). Gases (CH_4, O_2, and Ar) enter the grid under at constant velocity (1 atm and 25°C) and travel 5 cm (upstream region) to the front heat shield under developing laminar flow. Ceramic foam sections (front heat shield, catalyst, back heat shield, all 19 mm diameter by 10 mm long) were modeled using a homogeneous porous media approximation, which assumes local thermal equilibrium between gas and surface.[50] Porosity was taken as 0.81,[51] and the foam's solid component was simulated as polycrystalline α-alumina. Source terms were employed using the hydraulic diameter approach to account for pressure drop by inputting isotropic inertial and viscous resistance terms for 80-ppi ceramic foams.[52] Thermal conductivity in the porous zones was treated as an average between gas and surface based on porosity.

After leaving the back heat shield, gases travel 5 cm under developing laminar flow to the grid outlet. The boundary condition on external surfaces of the quartz tube was adiabatic. Surface chemistry in the porous catalyst section was included with a 38-step surface mechanism for CH_4 oxidation and reforming on Rh.[12] Temperature-dependent transport properties in the gas phase were calculated using kinetic theory, and effective thermal conductivities of the quartz (fused silica) and α-alumina were taken as polynomial functions of temperature.[47,48] Fickian diffusion was included using a mixture-averaged dilute diffusion coefficient for each species. The effect of the porous medium on diffusion was included by multiplying the dilute diffusion coefficient by the ratio of porosity to tortuosity. A value of 1.5 was used for tortuosity based on foam measurements.[53] The effect of

radiation in the calculation of the porous medium's effective thermal conductivity was neglected as it should be small on 80-ppi foams when compared to lower cell density foams (e.g., 10–45 ppi foams) with a smaller extinction coefficient[54] or packed beds with a significantly larger thermal conductivity.[55] To demonstrate this point, Sweeting et al.[56] give an effective thermal conductivity for a 45 ppi, 92% alumina foam (including the effects of conduction and radiation) of 1.28 W/(m K) at 1000°C. Effective thermal conductivity in this work for a 45 or 80 ppi foam is 1.3 W/(m K) at 1000°C. Neglecting the radiation effect becomes a better approximation as ppi and extinction coefficient of the foam increase. A previous numerical study using a 1D heterogeneous code to model methane oxidation on Pt/MgO found no significant contribution from radiation.[57] A recent 2D analysis confirms this finding for methane CPO in a honeycomb Rh catalyst.[58]

Converged solutions were acquired by solving the Navier-Stokes momentum, energy, and species continuity equations with a segregated, implicit solver[50] using a computational node on an IBM Power 4 system at the University of Minnesota. Species coverages were computed by coupling species continuity equations with wall surface reaction boundary conditions via a stiff, coupled solver.[50] A specific surface area of 160 cm^{-1} was used for the porous catalyst foam without additional tuning for comparison with PFR simulations. Geometric surface areas for 80-ppi foams up to 210 cm^{-1} have been estimated with no additional washcoat.[51] Using a standard underrelaxation method, ~100,000 iterations and 10–15 h were required for convergence. A criterion of 10^{-6} was used for each scaled residual component (continuity, r-velocity, z-velocity, energy, and species) to determine solution convergence. Solution results using convergence criteria ranging from 10^{-6} to 10^{-7} showed no significant difference in velocity, temperature, or concentrations (<1.0%), thereby validating the sufficiency of the criteria. Computational cell number for the hexahedral grid in these simulations was varied to ensure the solution was grid independent. In addition, the second-order discretization scheme in Fluent was utilized to reduce the effects of numerical diffusion (discretization error) on the solution.[50]

Surface mechanisms

38-Step Mechanism. Simulations (PFR or 2D) utilized a 38-step surface chemistry mechanism for methane oxidation on Rh[12,13] that has been validated against integral steady-state[12,25] and transient experimental data.[13,26] The mechanism in its current form is an improved version of the original mechanism for high temperature oxidation.[9] The mechanism was revised to include steam reforming and WGS and CO_2 readsorption,[12,22] which gave excellent agreement with integral steady-state data.[12] Coverage-dependent desorption energies for CO and O_2 were later included,[13] because they are important for lightoff agreement. Gas-phase chemistry is negligible at atmospheric pressure conditions for methane CPO[10,11,20] and was not included in the simulations. Intrinsic catalyst activity is included through the assumed site density for the Rh surface, which was 2.72×10^{-9} mol/cm^2 for the mechanism, and the geometric surface area-to-volume ratio of the catalyst (160 cm^{-1}).[51] Hereafter, the 38-step mechanism is designated Mechanism 1.

104-Step Mechanism. A much larger C_1 mechanism on Rh (104 reactions) was recently reported by Mhadeshwar and Vlachos.[27] Simulations were performed with this mechanism utilizing a PFR code based on CHEMKIN III architecture, which was provided by the mechanism's authors (Mhadeshwar AB and Vlachos DG, University of Delaware, personal communication, 2006). Kinetic parameter calculation with the UBI-QEP method is performed on-the-fly with the code causing solution time to increase significantly over the 38-step mechanism. In this work, the surface to volume ratio was kept at 7500 cm^{-1} as was used previously[27] to fit experimental spatial data,[36] and Rh site density was kept at 2.49×10^{-9} mol/cm^2 as set by the authors. Hereafter, the 104-step mechanism is designated Mechanism 2.

Results

PFR simulations based on experimental temperature profiles

Figure 2 displays the species profiles generated by using the experimental temperature field measured under high-resolution sampling as model input for $C/O = 1.0$ and total flow rate = 5 slpm.

The onset of O_2 conversion for both mechanisms, Model 1 (0.3 mm) and Model 2 (0.6 mm), is significantly delayed in comparison to the experiment where O_2 conversion starts right from the catalyst entrance. After onset, Mechanism 1 and the experimental profile converge to complete O_2 conversion by 1.3 mm whereas Mechanism 2 predicts total O_2 conversion slightly later at 1.5 mm (Figure 2A). CH_4 conversion behaves similarly for both mechanisms and both predict the same conversion at the catalyst exit, which is slightly lower than found by experiment (Figure 2A). Onset of syngas production is significantly delayed for Mechanisms 1 and 2 (0.5 vs. 1.4 mm, respectively) (Figure 2B). H_2 flow for Mechanism 2 reaches nearly the experimental value by 10 mm while Mechanism 1 lags behind; however, initial H_2 production for Mechanism 1 starts at an earlier distance than Mechanism 2. The same qualitative behavior is found for CO, but Mechanism 1 better predicts the outlet CO value. In contrast to the experiment where H_2 and CO are formed at comparable rates in the oxidation zone, Mechanism 1 predicts a faster CO formation. Both models capture peaking of H_2O flow rate and the step like behavior of the CO_2 flow rate qualitatively, but quantitative agreement with the experimental profiles is poor (Figure 2C).

The experimental data show that ~44% of the H_2 and ~67% of the CO are made in the presence of O_2. For Mechanism 1, only about 6% of H_2 and 29% of CO are made in the presence of O_2. Even less H_2 and CO are made in the presence of O_2 according to Mechanism 2 (6% and 9%, respectively).

Figure 3 highlights species coverages ($>10^{-6}$) for both models. Over the catalyst length Mechanism 1 shows a progression from initially O-covered to C- and Rh-covered with the major coverages ($>10^{-2}$) being Rh, C, CO, and H within 10 mm (Figure 4A). Mechanism 2 shows qualitatively similar coverage behavior; however, the shift in coverages occurs much more rapidly with an impulse-type behavior found at ~1.4–1.5 mm, the location of complete O_2 conversion (Figure 3B). The major outlet coverages for Mechanism 2

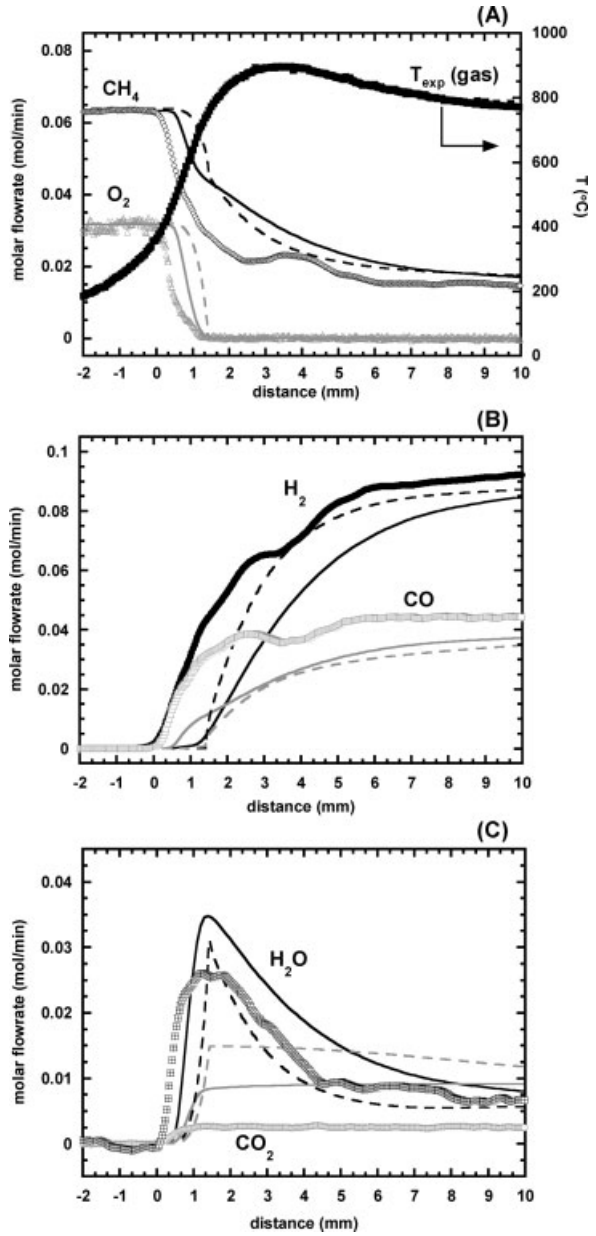

Figure 2. PFR species profiles based on experimental T profiles (5 slpm and *C/O* = 1.0).

Solid and dashed lines indicate simulations with Mechanisms 1 and 2, respectively.

are Rh, H, CH, and CH_2. Both mechanisms predict an entrance section of nearly full O coverage that corresponds to the delay in reactant conversion (Figure 2A).

Adiabatic PFR simulations

Effect of Inlet Temperature on Oxidation Section Length. Mechanism 1 was tuned based on surface/volume ratios of 80–210 cm^{-1}, which are typical values for the geometric surface area per unit volume of 45–80 ppi foams. However, Mechanism 2 was used with a surface/volume ratio of 7500 cm^{-1} (Ref. 27) as a fitting parameter for previous experimental spatial data.[36] Figure 2 shows that both mechanisms give similar performance with the experimental temperature profile when surface/volume ratios of 160 and 7500 cm^{-1} are used, respectively. Therefore, surface to volume ratios used previously for both mechanisms were not modified in this study.

To compare the reactivity of the two mechanisms the effect of inlet temperature on the adiabatic PFR models has been investigated. Since an adiabatic PFR model does not include the effect of upstream heat transport, the inlet temperature is a critical parameter for model performance. The oxidation length for Mechanism 1 with coverage dependence (of the activation energy for CO and O_2 desorption) is shorter than for Mechanism 2 for temperatures <825 K (Figure 4). Above this temperature, this trend reverses. Furthermore, the oxidation length for Mechanism 1 with coverage dependence is shorter than Mechanism 1 without coverage dependence until ~800 K, where the curves converge (Figure 4). To enable a performance comparison with the adiabatic PFR model, the inlet temperatures for Mechanism 1 with coverage dependence and Mechanism 2 were chosen as ~770 and 815 K, respectively, to guarantee an equivalent but arbitrary 0.5 mm oxidation length for both (Figure 5).

Temperature, Species, and Coverage Profiles: C/O = 1.0. Mechanisms 1 and 2 show similar qualitative perform-

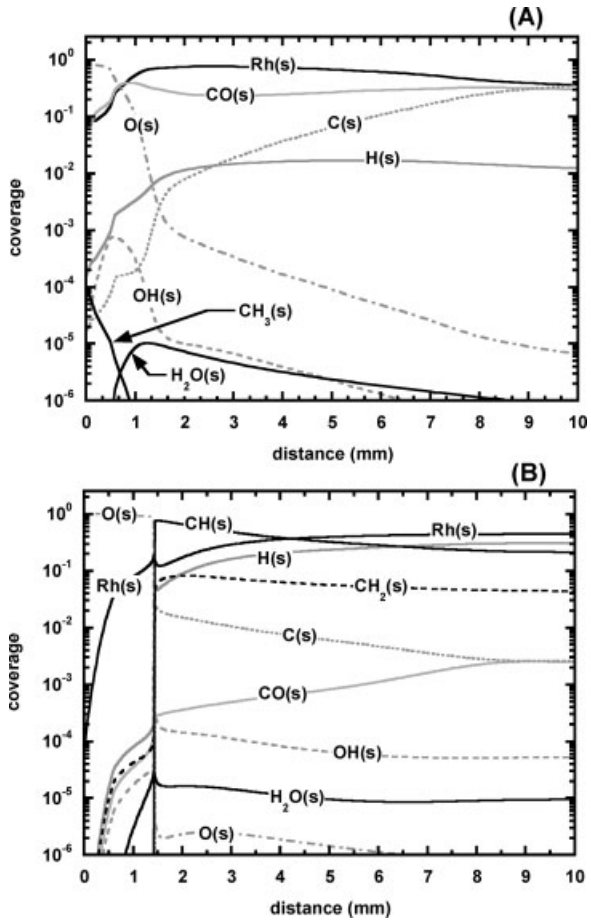

Figure 3. PFR coverages based on experimental T profiles (5 slpm and *C/O* = 1.0) for (A) Mechanism 1 and (B) Mechanism 2.

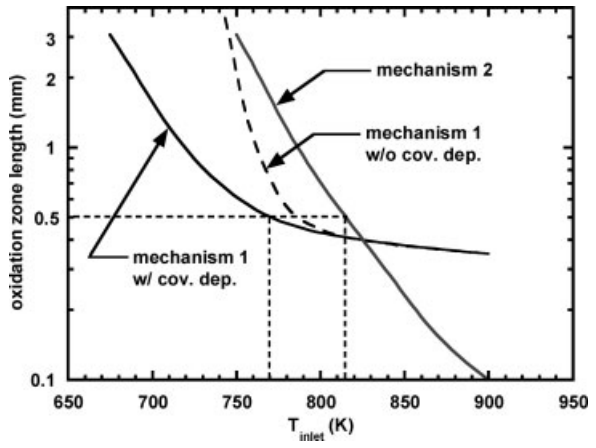

Figure 4. Effect of inlet temperature on oxidation zone length (99.9% oxygen conversion) for adiabatic PFR simulations with Mechanisms 1 and 2.

Reactor condition: 5 slpm total flow rate and $C/O = 1.0$.

ance under adiabatic conditions with pronounced exothermic oxidation and endothermic reforming zones; however, these zones develop much faster with Mechanism 2 (Figure 5). The temperatures in the oxidation zone quickly rise to 1380 and 1580°C for Mechanisms 1 and 2, respectively (Figure 5A), in agreement with the disappearance of O_2 (Figure 5B). Temperatures in the reforming zone then decrease to ~800°C for both (Figure 5A). Temperature in the reforming zone for Mechanism 2 decays much faster than Mechanism 1. CH_4 consumption occurs more quickly for Mechanism 2. Both mechanisms overpredict the experimental CH_4 outlet conversion significantly (Figure 5B).

Syngas production is drastically overpredicted by both models in comparison with experiment (Figure 5C) because both models overpredict the amount of steam reforming occurring (Figures 5B, D). This trend is even more pronounced for Mechanism 2 than for Mechanism 1. Mechanism 1 predicts CO_2 is formed mainly in the oxidation zone and is inert thereafter (Figure 5D). Mechanism 2 indicates some CO_2 reforming after the oxidation zone (Figure 5D inset), which is not experimentally observed.

The relative amounts of syngas produced in the oxidation zone (direct production) for both mechanisms follow the same trend as for the PFR model with the experimental temperature profile. Only the absolute numbers are higher because of the higher temperatures in the oxidation zone resulting from the adiabatic boundary conditions. As in Figure 2A, initial H_2 production for Mechanism 1 starts at an earlier distance than Mechanism 2. For Mechanism 1, ~40% of H_2 and 60% of CO are made in the presence of O_2. For Mechanism 2 only ~9% of H_2 and 30% of CO are made in the presence of O_2.

Figure 6 highlights the coverages ($>10^{-6}$) for both mechanisms. Over the catalyst length Mechanism 1 shows a pro-

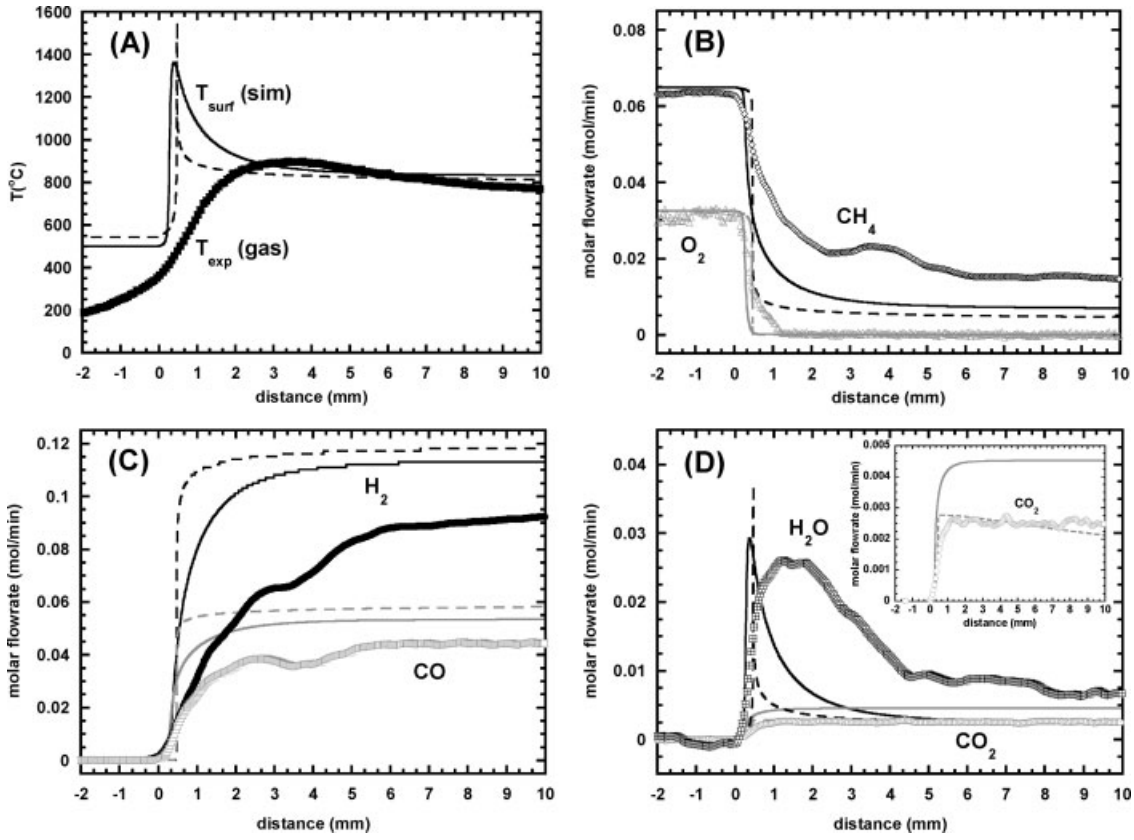

Figure 5. Adibatic PFR species profiles (5 slpm and $C/O = 1.0$).

Solid and dashed lines indicate simulations with Mechanisms 1 and 2, respectively.

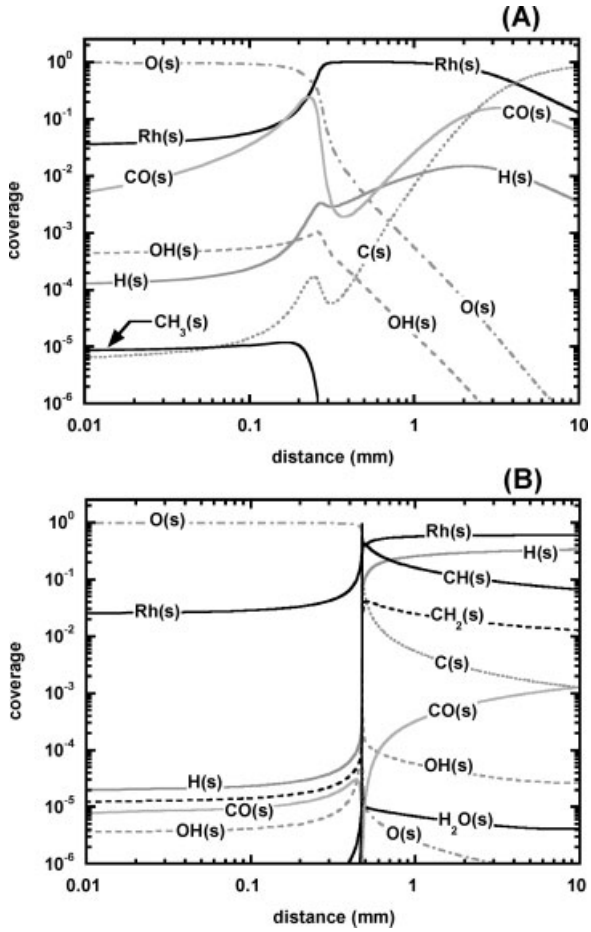

Figure 6. Adiabatic PFR species coverages based (5 slpm and *C/O* = 1.0) for (A) Mechanism 1 and (B) Mechanism 2.

gression from an initially O covered surface (0–0.2 mm) to a bare Rh surface (0.3–3 mm) to a partly C-covered Rh surface towards the end of the catalyst. Mechanism 2 again shows discontinuous changes in coverage at the location of complete O_2 conversion at 0.5 mm. Before the discontinuity the surface is essentially O covered, after the discontinuity the surface is ~50% free and the remaining sites are covered by H, CH, and CH_2 with H being the dominant surface species (coverage ~25%).

Temperature, Species, and Coverage Profiles: C/O = 0.7 and 1.3. Examining mechanism performance at $C/O = 0.7$ (fuel-lean) and 1.3 (fuel-rich) elucidate the ability of multistep chemistry to simulate catalyst behavior away from syngas stoichiometry at $C/O = 1.0$, where most mechanism validation has been performed. For $C/O = 0.7$, surface temperatures become much higher than $C/O = 1.0$ with peak temperatures of ~1580–1600°C for both mechanisms (Figure 7A). Even though Mechanisms 1 and 2 predict similar CH_4, O_2, H_2, and CO exit flow rates under adiabatic conditions at $C/O = 0.7$, the development lengths of the oxidation and reforming zones are slightly different (Figures 7B–D).

The oxidation and reforming zones for Mechanism 2 are extremely sharp and all chemical reactions are finished within 0.7 mm of the catalyst. Temperature rapidly decays for Mechanism 2 down to 1215°C at 0.625 mm along with complete consumption of CH_4 and O_2 (Figure 7B). H_2 and CO reach their exit flow rates within 0.7 mm (Figure 7C) accompanied by a rapid production and then consumption of H_2O (Figure 7D). Partial and total oxidation as well as steam reforming occurs practically simultaneously in Mechanism 2. In addition, CO_2 flow reaches its final value within 0.75 mm (Figure 7D).

In contrast, Mechanism 1 shows continuous oxidation and reforming zones. Temperature in the oxidation zone reaches 1580°C by 0.75 mm (Figure 7A) along with peak H_2O flow (Figure 7D) and complete consumption of O_2 (Figure 7B). Steam reforming continues until ~4 mm where methane conversion reaches completion. As indicated by the increasing CO_2 and H_2 flow rates and decreasing CO and H_2O flow rates, WGS is predicted to occur to a much greater extent with Mechanism 1 than found experimentally.

For $C/O = 1.3$, peak surface temperatures are lower (~1225°C for both mechanisms, Figure 7E) compared to $C/O = 1.0$. For Mechanism 1 the temperature reaches its final value of 900°C at 1.25 mm, whereas temperature continuously decreases over the remaining catalyst length for Mechanism 2 in agreement with the experimental temperature after 3 mm. As the inlet temperatures were adjusted to give the same oxidation zone lengths at $C/O = 1.0$ (0.5 mm, Figure 4), these inlet temperatures lead to similar oxidation zone lengths at $C/O = 0.7$ and 1.3 for the two mechanisms. Both mechanisms predict oxygen conversion too fast as well as too high CH_4 conversion (Figure 7F). As a result, H_2 and CO flow rates are overpredicted (Figure 7G). For $C/O = 1.3$, both mechanisms predict significantly more steam reforming than is experimentally observed (Figure 7F). CO_2 agreement with Mechanism 1 is reasonably good with no CO_2 reforming or WGS apparent in agreement with the experimental profile (Figure 7H). Mechanism 2 predicts some CO_2 reforming (Figure 7H inset).

Panels A-D of Figure 8 display the corresponding surface coverages ($>10^{-6}$) for $C/O = 0.7$ and 1.3, respectively. For $C/O = 0.7$ both mechanisms predict similar surface coverages, close to 100% O coverage at the catalyst entrance (0–0.5 mm) followed by an essentially bare Rh surface from 0.5 to 10 mm. Mechanism 2 predicts about 15% H coverage in the latter region. The situation is more diverse at $C/O = 1.3$. Mechanism 1 predicts three distinct zones. An O-covered zone from 0 to 0.1 mm, a bare Rh surface from 0.2 to 1 mm and a C-covered surface from 1.5 mm until the end of the catalyst. Mechanism 2 predicts full O coverage until 0.4 mm where a discontinuous coverage change leads to a mainly Rh covered surface partly covered with CH, H, and CH_2.

2D simulations with 38-step mechanism

Because neither of the PFR models captured the experimental species and temperature profiles satisfactorily, 2D computations were used to test whether the reaction mechanism or the reactor model was inadequate for the mathematical description of the system. Because of the inherent complexity of Mechanism 2 and portability challenge in a CFD code, only Mechanism 1 was tested to simulate species and temperature profiles on Rh for experimental GHSV of $2.6 \times 10^5\ h^{-1}$ (total inlet flow = 5 slpm) and atom feed ratios of

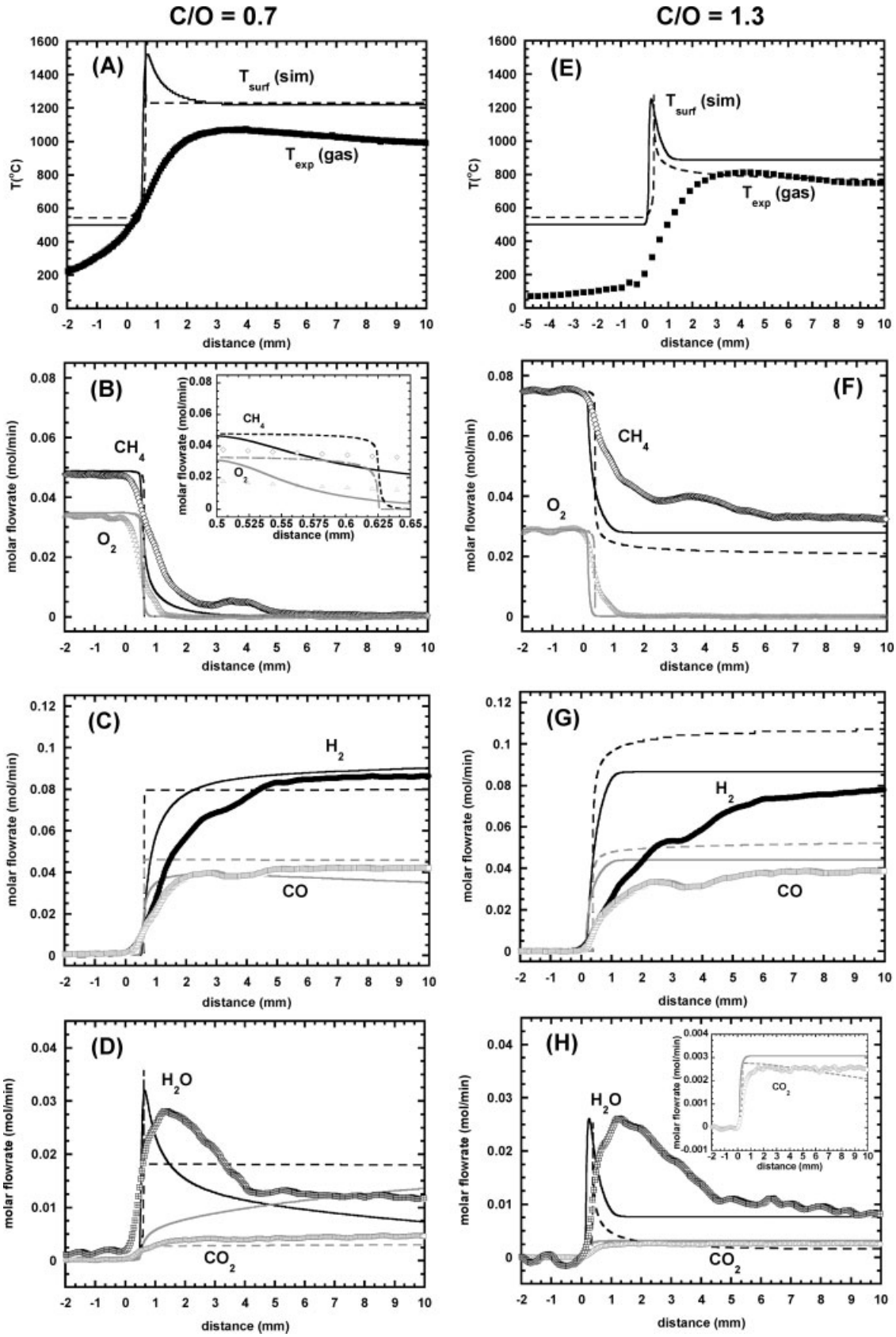

Figure 7. Adiabatic PFR species profiles (5 slpm, *C/O* = 0.7 and 1.3).

Solid and dashed lines indicate simulations with Mechanisms 1 and 2, respectively. Panels A–D correspond to $C/O = 0.7$; panels E–H correspond to $C/O = 1.3$.

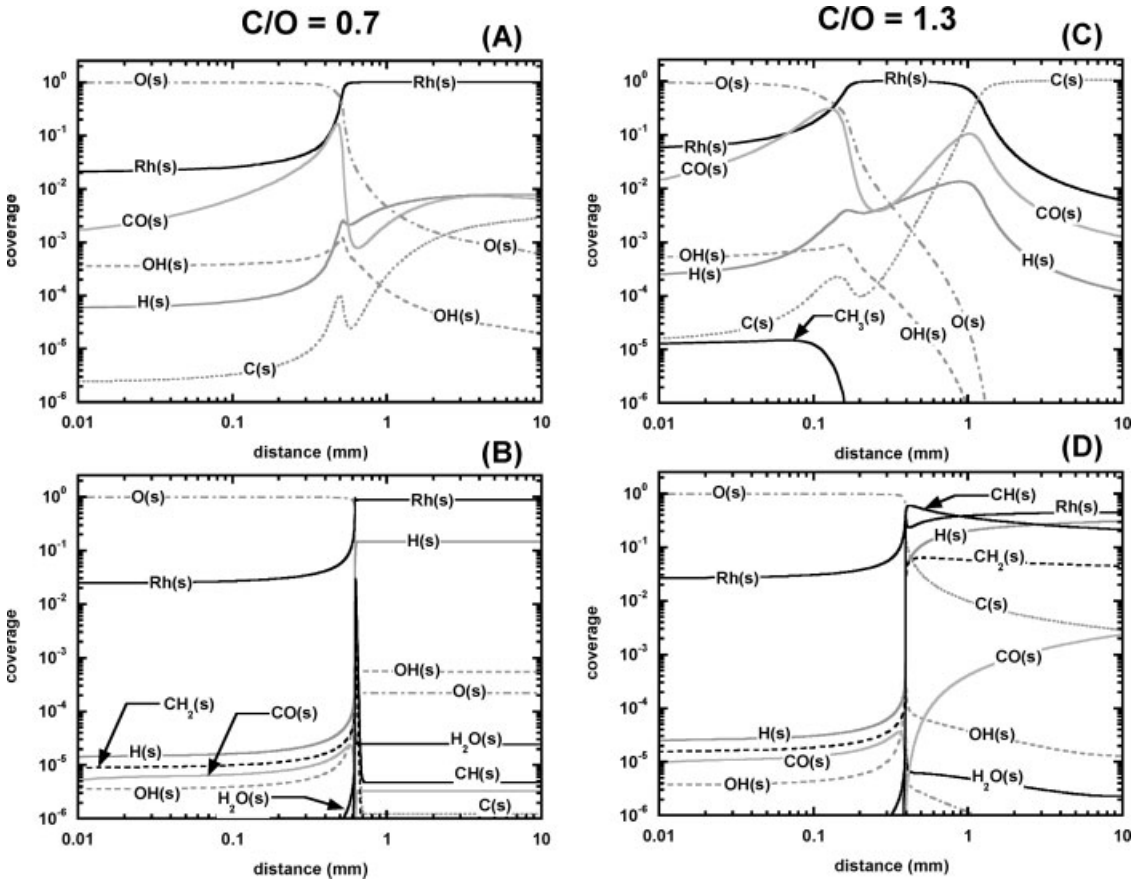

Figure 8. Adiabatic PFR species coverages (5 slpm, *C/O* = 0.7 and 1.3).

Panels A, B correspond to $C/O = 0.7$; panels C, D correspond to $C/O = 1.3$. (A, C) Mechanism 1. (B, D) Mechanism 2.

$C/O = 0.7$, 1.0, and 1.3. Figure 9 highlights the 2D temperature, velocity, and species profiles for Mechanism 1 using the 2D porous model. Only half the domain given in Figure 1 is considered because of axial symmetry. Figure 10 presents a performance comparison of the 2D channel model versus the 2D porous model. Significant gradients in the radial direction (Figure 9) are observed for the porous model profiles because of axial heat transport in the quartz reactor wall. Centerline profiles for $C/O = 1.0$ are displayed in Figure 10 allowing a direct comparison with the centerline experimental data. Figure 11 displays the predicted profiles for the superior 2D porous model at $C/O = 0.7$ and 1.3. Surface coverages for all C/O ratios are shown in Figure 12.

Temperature and Species Profiles: C/O = 1.0. 2D profiles for temperature, velocity, and species compositions for the 2D porous model reveal that radial gradients are noticeable because of axial heat transport through the quartz reactor wall (Figure 9). The quartz tube has some entrance effects on the flow as it conducts heat from the catalyst section upstream and warms up the entering gases close to the wall. Radial gradients smooth as the flow exits the catalyst.

Comparison of the 2D channel and porous models (Figure 10) indicates the porous model matches the experimental data better than the channel model (discussed later). However, in comparison to simple PFR models both 2D models are in much better agreement with the experimental data.

As shown for the porous model in Figure 10, the calculated surface temperature increases from ~600°C at 2 mm within the front heat shield to 1000°C at the catalyst entrance. All of the oxygen and 40% of methane are converted within 0.5 mm (oxidation zone) where H_2O and CO_2 flow rates reach their maximum values. The oxidation zone is noticeably shorter than found experimentally (~1.3 mm). The amounts of H_2 and CO produced in the oxidation zone, 40% (0.035 mol H_2/min) and 58% (0.026 mol CO/min) of total, respectively, are in good agreement with the experimental data, 45% (0.042 mol H_2/min) and 67% (0.03 mol CO/min) of total. In the reforming zone, the CH_4 and H_2O continue reacting to give significant production of more syngas through steam reforming accompanied by a decrease in the calculated temperature from 1000°C at the end of the oxidation zone to 735°C at the catalyst exit. In agreement with the experiment, the simulations show no sign of CO_2 reforming or WGS under these conditions. The calculated surface temperature and experimental gas temperature equilibrate at ~2 mm, and calculated temperature falls below the experimental temperature for the remaining catalyst length.

Temperature and Species Profiles: C/O = 0.7 and 1.3. Comparison of the 2D porous model with the experi-

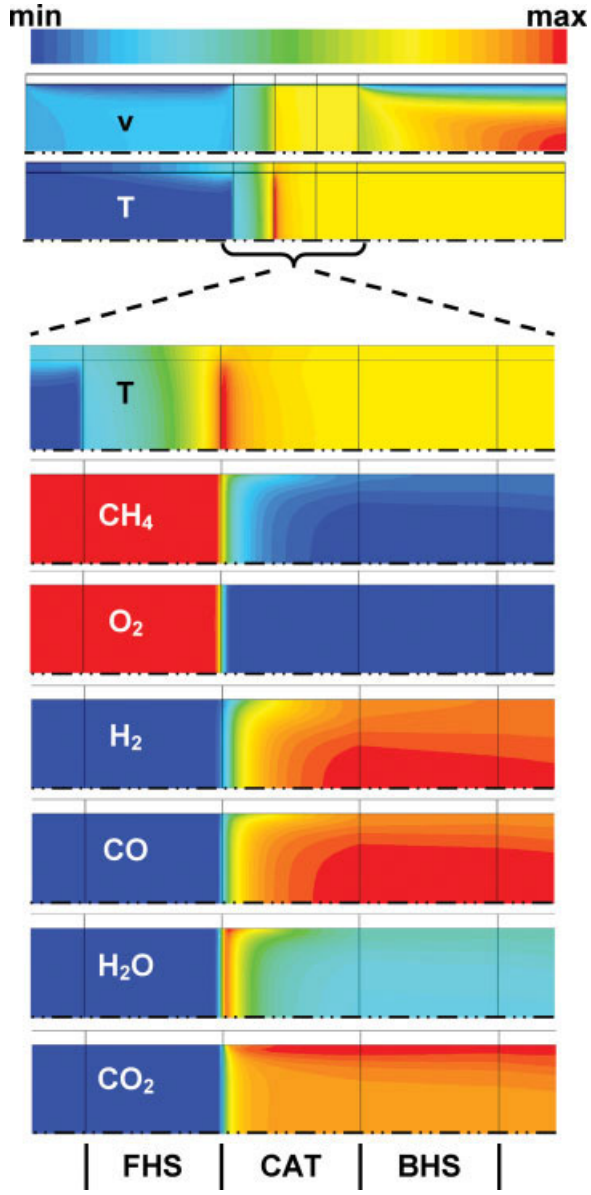

Figure 9. Contour plots of temperature (T), velocity magnitude (v), and molar flows for adiabatic 2D porous media model (5 slpm and *C/O* = 1.0).

Only the top half of the domain shown in Figure 1 is simulated because of axisymmetry. T and molar flows are shown as a close up for the foam monolith stack. Min/max ranges: *T*: 25–990°C, *v*: 0–2.24 m/s, CH_4: 0.0131–0.063 mol/min, O_2: 0–0.0316 mol/min, H_2: 0–0.0904 mol/min, CO: 0–0.0459 mol/min, CO_2: 0–0.00454 mol/min, H_2O: 0–0.0338 mol/min.

mental data for the two other investigated stoichiometries is presented in Figure 11. The simulations match the experimental data similarly well as with $C/O = 1.0$, but some quantitative discrepancies are observed.

For $C/O = 0.7$, the catalyst runs considerably hotter and the calculated surface temperature rises from ~700°C at 2 mm in front of the catalyst to ~1200°C at the catalyst entrance (Figure 12). Steam reforming causes the temperature to decline to ~1050°C at the end of the catalyst. All of the oxygen and ~68% of methane are converted within 0.5 mm of the catalyst (oxidation zone). Oxidation zone length is still shorter than found experimentally; however, the simulation shows correctly that the length of the oxidation zone does not change by going from $C/O = 1.0$–0.7. The amounts of H_2 and CO predicted to be formed in the oxidation zone at these higher temperatures, 50% (0.042 mol H_2/min) and 73% (0.0275 mol CO/min) of total, respectively, are again in close agreement with the experimental values, 56% (0.0475 mol H_2/min) and 76% (0.0325 mol CO/min) of total, respectively. H_2O flow rate peaks at the end of the oxidation zone and decreases in the steam reforming zone. The model overpredicts secondary H_2O consumption, not by overpredicting steam reforming but rather by overpredicting WGS as reflected in the rising CO_2 flow rate. The prediction of WGS is the major disagreement between model and experiment for low *C/O* ratios. The calculated surface temperature and experimental gas temperature equilibrate after ~3 mm, but the exothermic WGS outweighs somewhat the endothermic steam reforming preventing the simulated temperature to fall below the experimental temperature in the steam-reforming zone.

For $C/O = 1.3$, the catalyst runs slightly cooler than at $C/O = 1.0$ and the temperature rises from ~550°C at 2 mm in front of the catalyst to ~875°C at the end of the oxidation zone (0.5 mm). As with $C/O = 1.0$ the calculated temperature falls below the experimental temperature in the steam-reforming zone, and both values converge to ~750°C at the end of the catalyst. The model predicts the same oxidation zone lengths (0.5 mm) as for $C/O = 0.7$ and 1.0. Independence of oxidation zone length from the *C/O* ratio is consistent with the experiments even though the difference between experimental and predicted oxidation zone lengths are for all *C/O* ratio ~0.8 mm. The amounts of H_2 and CO formed in the oxidation zone, 0.036 mol H_2/min (51% of total) and 0.025 mol CO/min (63% of total), respectively, are in good agreement with those found experimentally, 0.035 mol H_2/min (45% of total) and 0.026 mol CO/min (65% of total). The model predicts the outlet flow rates for CO, H_2O, and CO_2 well, but H_2 flow rate is underpredicted by 10%.

Species Coverages. The calculated major species coverages show a clear trend with changing *C/O* ratio from 0.7–1.0 to 1.3 (Figure 12). For $C/O = 0.7$ characterized by calculated surface temperatures always above 1000°C, the surface is essentially bare Rh with coverages varying from 0.975 at the catalyst entrance to 0.95 at the outlet. Down the catalyst axis, oxygen coverage decreases in the first 2 mm from ~2% to a fraction of a percent, while CO, H, and C increase in coverage from below ~1–3% to 1%, respectively, at the reactor outlet. As *C/O* ratio is gradually increased (surface temperature decreases) it turns out that C and CO become the only two important surface species with their coverages increasing much steeper than for $C/O = 0.7$. In the first 0.5 mm where the surface is hot (oxidation zone) more than 98% of the Rh sites are predicted to be uncovered, similar to $C/O = 0.7$. However, C and CO coverages rise quickly with declining surface temperature reaching 30 and 50%, respectively, for $C/O = 1.0$, and 88% and 7%, respectively, for $C/O = 1.3$. It can be summarized that the model predicts a clean surface at high temperatures and/or in the presence of O_2 and large amounts of H_2O ($C/O = 0.7$). For low tempera-

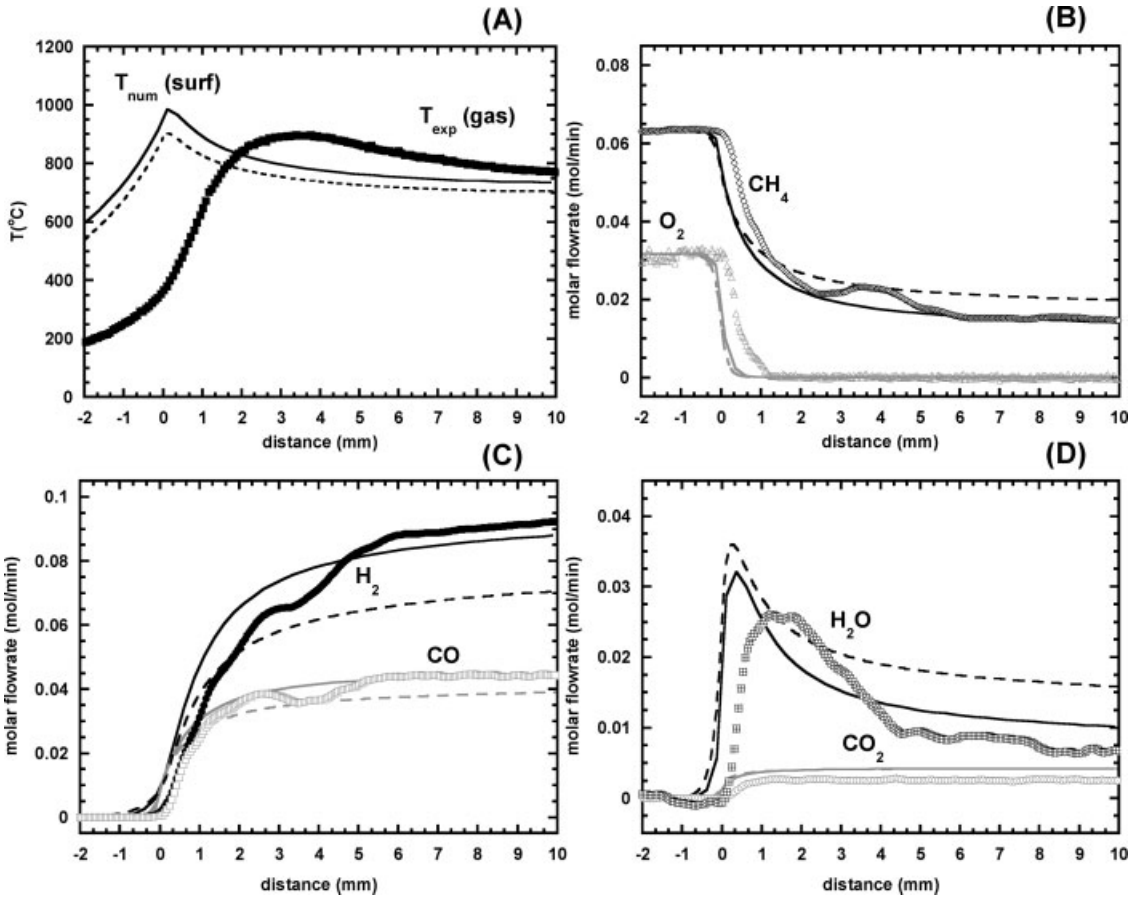

Figure 10. Centerline temperature and species profiles for 2D adiabatic models (5 slpm and *C/O* = 1.0).

Solid and dashed lines indicate simulations with the 2D porous media and pore channel models, respectively.

tures, absence of gas phase O_2 and low concentrations of water vapor, the surface is predicted to be carbon covered ($C/O = 1.3$). For syngas stoichiometry ($C/O = 1.0$), CO is predicted to be the major surface species in the second half of the catalyst with ~50% coverage.

Discussion

Total agreement between experimental profiles and numerical simulations could only be achieved if the experimental data were accurate, reproducible and free of artifacts, the reactor model mapped the experiment perfectly, and the multistep chemistry was valid for all experimental conditions investigated. In reality, experimental data are always subject to error, and the reactor model can never reproduce the experiment in every detail. As the goal of the present numerical study is to assess the validity of the applied reactor models and chemistry mechanisms, experimental uncertainty and uncertainties in model parameters deserve review before the predictive capabilities of the different models and the two mechanisms are discussed.

Experimental uncertainty

A measure for experimental accuracy is the atom balance error at each axial location. At steady-state, species accumulation does not occur and atom balance errors should be zero. The experimental profiles presented in this work for the species H_2, CH_4, CO, O_2, and CO_2 are mass spectrometry measurements (see experimental details described elsewhere[28,43]). The H_2O profile is calculated as a least squares optimization from the O and H atom balances. For the data presented in this work, the carbon atom balance closed for all points between −1 and +3%. The hydrogen atom balance is slightly biased towards positive values and ranges in an interval between +2 and +5%. As the least squares calculation weights the H atom balance twice as high as the O atom balance, the O atom balance combines most of the experimental uncertainty. However, it closes for all axial locations between −13 and +5%. The thermocouple reading is accurate to ±1%, but the measured temperature can be assigned neither to the catalyst temperature nor to the gas temperature. The thermocouple is enclosed in the quartz capillary and has direct thermal contact with the flowing gas but not with the catalyst surface. However, it sees radiation from the surface. The measured temperature is therefore largely biased towards the gas temperature, which has to be taken into account by comparing it to models, which have explicit surface and gas temperatures.

The reproducibility of the experimental profiles has been verified by performing independent profile measurements on different catalysts and different reactor setups. Axial meas-

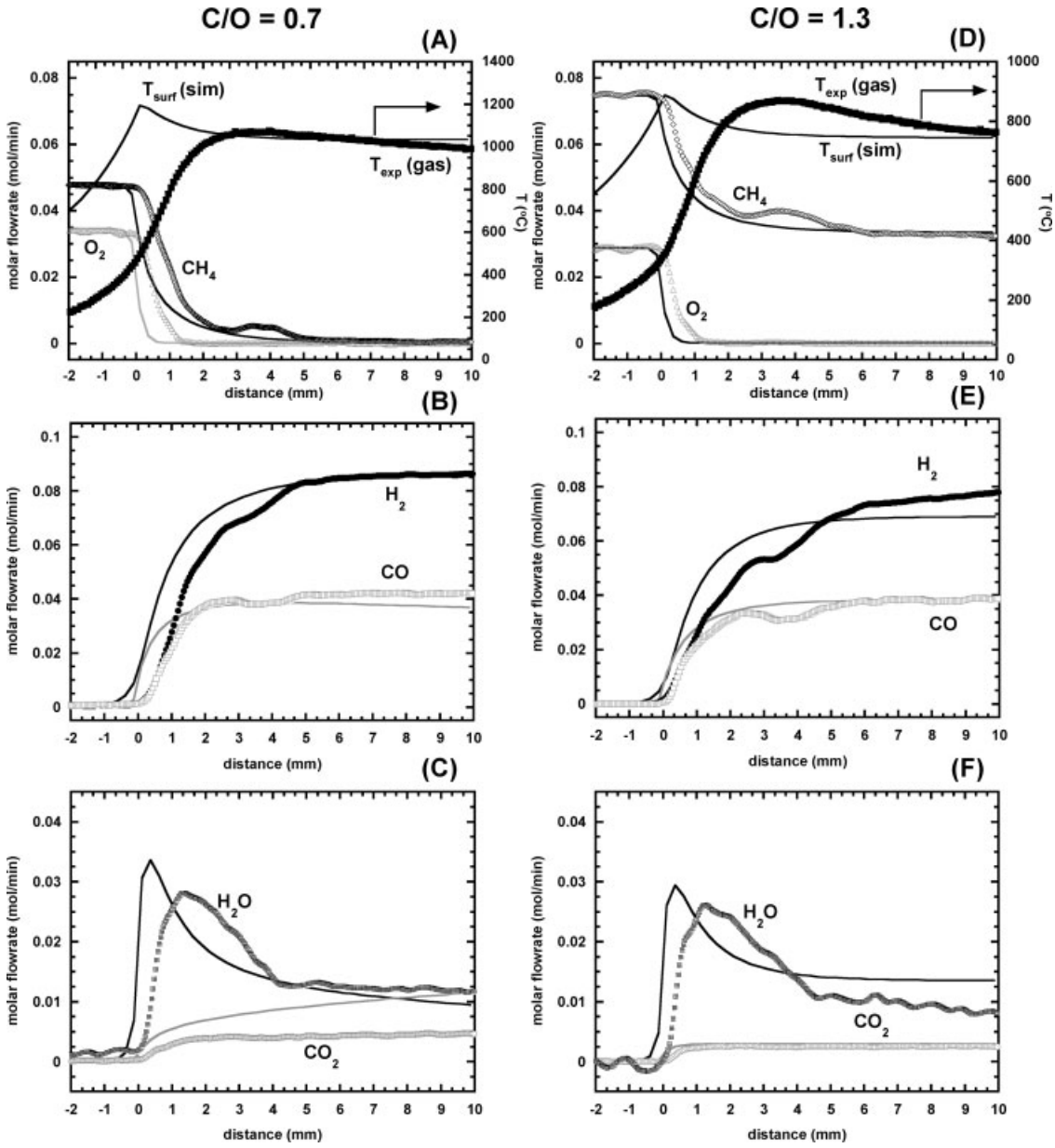

Figure 11. Centerline temperature and species profiles for 2D adiabatic porous model (5 slpm and $C/O = 0.7$ and 1.3).

Panels A–C correspond to $C/O = 0.7$; panels D–F correspond to $C/O = 1.3$.

ures (e.g. length of the oxidation zone) can be reproduced to within 1 mm. Species concentrations at the reactor outlet were reproducible to ~5%. The fine plateaus, bumps, and spikes observed in most of the profiles are only partly reproducible. Some of the fine structure may be caused by the random structure and size distribution of the pores in the foams. Pockets or blocked pores along the capillary channel or even back mixing effects caused by the pore structure around the channel can lead to features in the profile that can never be captured by the model, which assumes a well defined or idealized flow profile. In the discussion of the performance of the investigated reactor models and mechanisms only deviations that are significant with respect to the aforementioned experimental uncertainties will be discussed.

Uncertainty in model parameters

A number of parameters enter the model for which reasonable guesses have to be made. Whereas a comprehensive sensitivity analysis of their influence is beyond the scope of this work, the most important parameters and their chosen values will be discussed below.

Pore Diameter. All reactor models require the specification of a pore diameter. In this work, a pore diameter of 0.25 mm was used, which is the mean pore diameter found from experimental visualization for an 80-ppi foam.[51] However, a foam possesses a large range of pore diameters, which are typically normally distributed for moderate ppi foams (10–65 ppi).[51] Being restricted to a single channel diameter in these

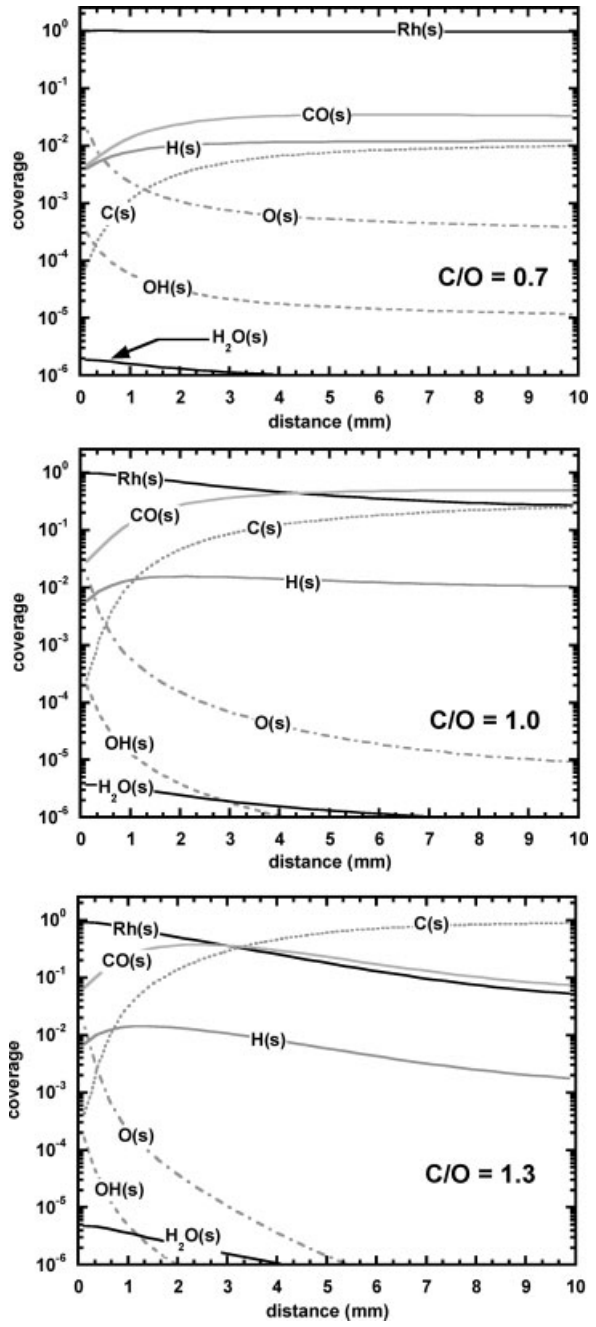

Figure 12. Centerline species coverages based for 2D adiabatic porous model (5 slpm and *C/O* = 0.7, 1.0, and 1.3).

simulations is a drawback since the flow encounters many pore diameters as it traverses the foam. Residence time distribution and heat transfer are strong functions of the pore diameter distribution, which most likely widens as ppi is increased. A larger pore diameter in a channel model for example increases the length that is required for the gas and surface to equilibrate. Figure 13 shows the results of simulations with the boundary-layer code Creslaf[59] coupled with Mechanism 1. As the channel diameter increases from 0.25 to 2 mm, the equilibration length increases from less than 0.5 to ~7 mm. For the 2D models, inlet discrepancies are most likely caused by the assumption of thermal equilibrium in the catalyst, which is not valid in the oxidation zone. Since the gas-phase temperature is overpredicted, mass diffusivity is also overpredicted and some back-diffusion occurs in the model, which is observed for both the porous and channel models.

Foam Tortuosity. Another critical parameter in the porous model becomes the tortuosity, which is the ratio between the actual length the gases travel through the foam to the length of the foam. The effect of tortuosity is to limit mass diffusion in the porous zones and to increase the pressure drop. The value of 1.5 used in this study was based on experimental measurements with 8–45 ppi foams,[53] where there appears to be a strong power law dependence between ppi and tortuosity. However, the tortuosity for an 80-ppi foam may be much higher, and values between 1.5 and 5 have been measured for similar pore densities.[60] Increasing the tortuosity value in the porous model simulations from 1.5 to 4 improves the agreement between experiments and simulations in the first 3 mm of the catalyst (data not shown).

Interphase Heat and Mass Transport. It should be mentioned again that the porous model in this work has considered the catalyst as a homogeneous medium and the calculated species profiles shown here do not include the effect of interphase transport but only depict the performance of the multi-step chemistry. Mass and heat transfer correlations for lower ppi foams (15–45) have been measured, but may not be reliable for higher ppi foams because of the inconsistency in the pore structures as ppi increases. Nevertheless, inclusion of heat and mass transfer correlations in a two-zone (heterogeneous) porous model would most likely improve the agreement in the oxidation section.

Catalytic Surface Area and Site Density. A final uncertainty is in the foam's catalytic surface area and the nature of the active sites. BET surface area is typically found to be ~1–2 m^2/g (specific surface area ~1.6×10^4 cm^{-1}) for a blank foam[52] similar to those used in this work. The specific geometric surface area (4/d for cylinder) for an average pore diameter of 250 μm is ~160 cm^{-1} (i.e. ~100 times smaller). In this work, Mechanism 1 was used with 160 cm^{-1}, whereas Mechanism 2 was used with 7500 cm^{-1} (a factor of ~50 larger) as suggested by Mhadeshwar and Vlachos.[27] Mechanism 2 shows no reactivity at 160 cm^{-1} for typical inlet PFR temperatures shown in Figure 4. Mechanism 1 reacts much more rapidly at the higher 7500 cm^{-1} value.

The difference between BET surface and geometric surface is caused by the microstructure of the foam showing small cracks that increase the surface area. The addition of a metal with or without washcoat may lead to a film coverage with a catalytic surface close to the geometric surface area, as shown previously by surface characterization.[61] Assuming that every surface metal atom is a catalytic site and that the film is an extended Rh(111) surface leads to an estimate of the catalytic site density of ~2.7×10^{-9} mol/cm^2 as used in this work. However, metal dispersion on the surface can be a strong function of the surface free energy of metal and support, the metal loading, and the operation temperature. If the metal sinters and forms crystals under operation then site density may change as a function of time on stream. It is also debatable if one single atom can be considered as an

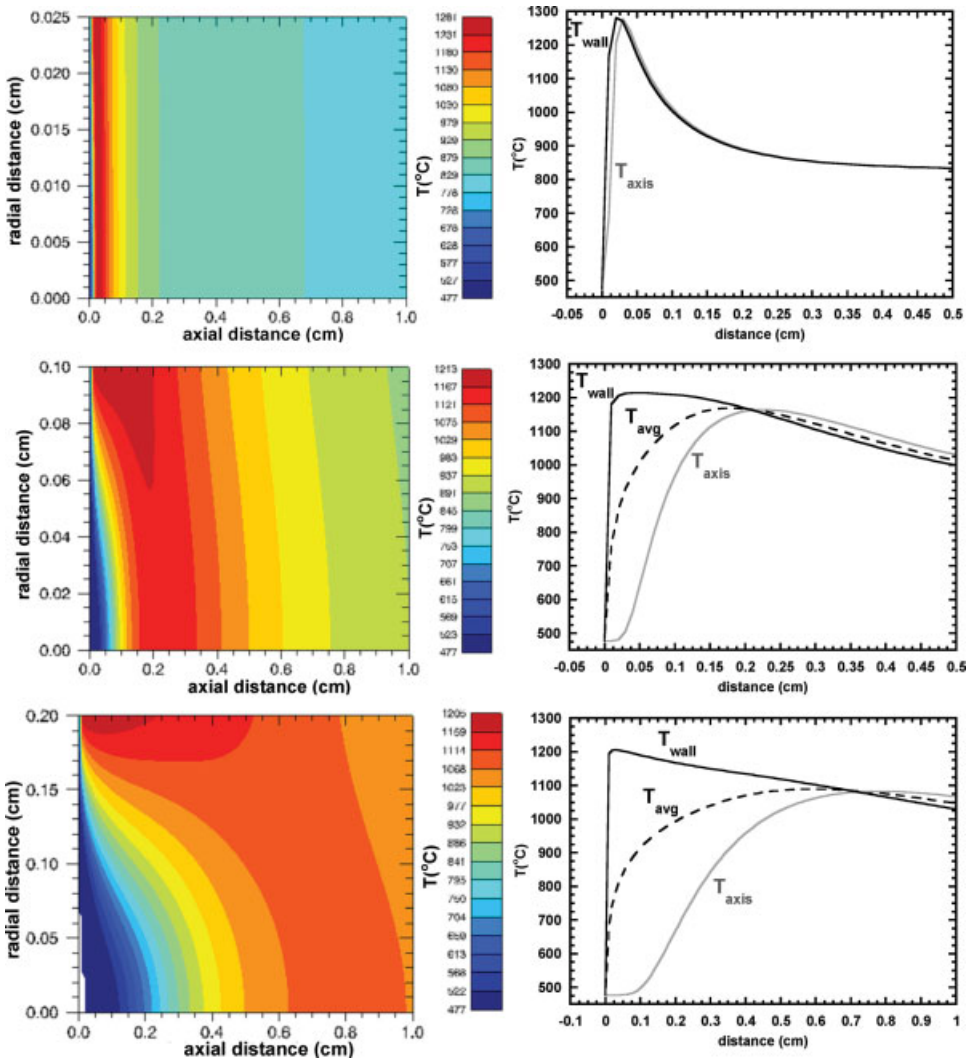

Figure 13. Effect of pore diameter on thermal entry length for methane CPO.

Adiabatic Chemkin boundary layer calculation for pore diameters of 0.25 mm (top panels), 1 mm (middle panels), and 2 mm (bottom panels). Inlet conditions are 5 slpm total flowrate, $C/O = 1.0$, $T_{in} = 750$ K, and $v_{in} = 80$ cm/s. T_{avg} and T_{axis} denote the area average gas-phase temperature and centerline temperature, respectively.

active site. Not considered in the model is loss of active sites due to multilayer carbon formation, in particular at the end of the catalyst. More characterization is needed to determine the catalyst surface area for foams under reaction conditions so that surface mechanisms can be tuned at the appropriate surface to volume ratio.

Comparison of PFR models and 2D models (Figures 2, 5, and 10)

Both reactor model and surface mechanism are critical to simulate the species development in the catalyst correctly. A comparison between adiabatic 2D and PFR simulations show that considering axial heat transport in the wall and in the gas is crucial. The adiabatic PFR model predicts a dramatically higher peak temperature than the 2D model and therefore shows an unreasonably fast development of the species profiles to their final steady-state values. A PFR model might be applicable if a correct experimental surface temperature profile could be provided (e.g. pyrometer measurements). However, an experimental temperature profile composed of thermocouple readings is strongly biased towards the gas phase temperature, which is in the oxidation zone much lower and in the reforming zone higher than the surface temperature. In summary, neither the PFR model with the experimental thermocouple profile nor the adiabatic PFR model could resolve the measured species profiles using either mechanism. The PFR profiles develop either too slow or too fast.

Comparison of 2D channel model and 2D porous model (Figure 10)

Correct simulation of the surface temperature profile is mandatory to reasonably predict species development in an autothermal foam catalyst. Including effects of axial heat conduction in the alumina support and the quartz tube in the model is important. Even if the solution of a PFR model

with a 1-cm long isothermal catalyst wall will approach the solution of a full 2D model by the reactor outlet,[62] it never will for an autothermal foam catalyst that features large temperature gradients. Neglecting the effect of wall heat conduction seriously affects the surface temperature[57] and predicted reactor yields.[63]

Axial heat conduction in the quartz tube and the alumina support is included in the 2D porous and channel model used in the present work; hence they show similar performance (Figure 10). The influence of the inlet temperature (25°C) is more severe on the channel model since the walls possess a higher thermal conductivity than in the porous model, and the channel model only comprises a hypothetical pore of the foam monolith stack (front heat shield, catalyst, back heat shield). Therefore, more heat is dissipated upstream and downstream resulting in a lower catalyst temperature and less steam reforming (CH_4 and H_2O flow rates higher, H_2 and CO flow rates lower than experiment).

Panel A in Figure 10 shows how the calculated temperatures of the 2D models compare to the experimental values measured with the thermocouple. As surface temperature dictates the chemistry only one energy equation is solved for both surface and gas (local thermal equilibrium). Together with the thermocouple measurements, the simulated profile and the experimental profile present together a set of surface and gas phase temperatures, respectively. Exothermic reactions raise the surface temperature in the oxidation zone sharply. The surface temperature maximum occurs near the catalyst entrance, even before oxygen is fully consumed, because endothermic steam reforming sets in as soon as water is formed. The incoming gases need some time to adjust to the hot surface, therefore the temperature profile measured with the thermocouple falls below the calculated surface temperature. After the surface temperature peaks, endothermic steam reforming pulls the surface temperature down leading to a cross over between surface and gas temperature at ~1.8 mm. After cross over the gas temperature remains higher than the surface temperature because of heat transfer limitations from the hot gases to the surface that is constantly cooled by steam reforming. These results are in line with previous simulations solving energy equations for both the gas and solid phases for fixed beds.[25,57] The authors also report large temperature gradients between gas and surface in the catalyst entrance region ($T_{sur} \gg T_{gas}$) with a cross over and a slightly higher gas phase temperature in the reforming zone.

For $C/O = 1.0$, the 2D porous model predicts the species and temperature profiles quantitatively within the experimental margins of error (Figure 10, panels A–D). The channel model captures the trends qualitatively but the absolute values are outside the experimental margins of error (e.g. H_2, CO, CH_4).

Comparison of 2D porous model and experimental profiles (Figures 10 and 11)

The 2D porous model with the 38-step surface mechanism (Mechanism 1) was applied to predict species and temperature profiles for $C/O = 0.7$, 1.0, and 1.3 at a 5-slpm inlet flow rate (Figures 10 and 11). Quantitative species agreement between experiments and simulations for the 2D porous model is good for all three C/O ratios, and only few significant differences are observed. The most apparent weakness of Mechanism 1 observed in this study is it predicts more WGS to occur at $C/O = 0.7$ than seen experimentally. This leads to an underprediction of the CO molar flow rate at the end of the catalyst (Figure 11B) and an overprediction of the CO_2 molar flow rate at the end of the catalyst (Figure 11C). At $C/O = 1.3$, the amount of steam reforming is slightly underpredicted leading to a higher H_2O and lower H_2 molar flow rate at the catalyst exit than found experimentally.

Simulations show clearly that surface Mechanism 1 predicts a mixed mechanism for syngas production: CO and H_2 are produced in the oxidation zone and in the steam reforming zone. This is in agreement with the experiment. The model also predicts correctly that the higher the temperature, the higher the amount of H_2 and CO produced in the oxidation zone from $C/O = 1.0$–0.7. Direct H_2 formation is less pronounced than direct CO formation, again in agreement with the experimental trend. Species profiles at the catalyst exit compare well with the experimental selectivities found in this work and in previous integral data comparisons.[12,25] Deviations between the experimental and predicted profiles in the first half of the catalyst and the length of the oxidation zone cannot be considered significant as the experimental profiles show variability from catalyst to catalyst.

Comparison of Mechanism 1 and Mechanism 2 (Figures 2–8)

A significant part of this work was devoted to the comparison of two state-of-the-art surface reaction mechanisms for the methane CPO on Rh.[12,27] As Mechanism 2[27] could not be used within a 2D channel or porous model, the comparison was accomplished within a PFR reactor model using either (i) experimental temperature profiles as input or (ii) treating the reactor as adiabatic. As the surface temperature is too low in case of using experimental thermocouple measurements as input (measures gas phase temperature) and too high in case of the adiabatic treatment, the species developments are either over- or underpredicted and only qualitative conclusions can be drawn.

There are two important differences between Mechanisms 1 and 2. Whereas Mechanism 1 (Ref. 12) predicts continuously developing species and surface coverage profiles over the entire length of the catalyst, Mechanism 2 (Ref. 27) predicts extremely sharp changes in species flow rates and surface coverages at the point of total O_2 conversion. This discontinuous behavior appears to be the result of the temperature and coupled coverage dependencies of activation energies for all surface reaction steps in Mechanism 2. The second difference is that Mechanism 2 predicts only small amounts of CO and almost no H_2 to be produced in the oxidation zone in contrast to Mechanism 1, which predicts significant direct syngas formation in agreement with the experimental profiles (Figures 2B and 5C). The performance of Mechanism 2 observed in this work is in agreement to what was found by Mhadeshwar and Vlachos themselves in an earlier comparison between simulation and experimental profiles.[27] In that work, the authors validated their mechanism against experimental spatial data[36] using the thermocouple temperature profiles as input. As in Figures 2 and 5, the

mechanism predicted a distinct oxidation zone (CO_2, CO, and H_2O are products) and a reforming zone (CO and H_2 are products). The authors concluded that H_2 was produced strictly in the reforming zone whereas CO was produced in both oxidation and reforming zone. This assertion was in disagreement with the conclusions of the authors of the experimental spatial study.[36]

In summary, Mechanism 1 embedded in a realistic reactor model (e.g. 2D porous model) predicts the experimental profiles within their margins of error. The only significant difference found between model and experiment was the overprediction of WGS at $C/O = 0.7$. Mechanism 2 was not used with a 2D model, however, the PFR simulations indicate that Mechanism 2 appears inferior to Mechanism 1 as it does not capture significant H_2 formation in the oxidation zone and predicts physically unlikely discontinuities at the point of total O_2 conversion.

Conclusions

Axial species profiles for methane CPO on autothermal Rh coated foam catalysts can be modeled accurately by combining a multistep surface reaction mechanism with a 2D reactor model capturing axial heat and mass transport. Best results were obtained with a 38-step surface reaction mechanism and a 2D porous model. Three inlet stoichiometries ($C/O = 0.7$, 1.0, 1.3) at 5-slpm inlet flow rate were investigated and the predicted profiles agree within the margins of error with the experimental profiles. However, at $C/O = 0.7$ the 38-step mechanism predicts significantly more WGS than experimentally observed. A PFR model employing either an experimental gas phase temperature profile or an adiabatic boundary condition was shown to be unsatisfactory because it does not capture the right temperature profile of the surface. A 2D channel model was significant better than the PFR model but still inferior to the 2D porous model because it over emphasized heat transport in the channel wall. Another more extensive surface reaction mechanism consisting of 104 surface reaction steps was found to predict exit flow rates similar to the 38-step mechanism within the PFR embodiment but it did not predict significant hydrogen production in the oxidation zone in contrast to the 38-step mechanism and the experimental profiles.

Acknowledgments

K.A.W. thanks the Minnesota Supercomputer Institute for the generous computational resources and partial support of this work. R.H. acknowledges funding through an Alexander von Humboldt Foundation Feodor Lynen Fellowship. The authors thank A.B. Mhadeshwar and D.G. Vlachos for generously sharing their C_1 mechanism on Rh coupled with the PFR code.

Literature Cited

1. Ahlbrandt TS. Future petroleum energy resources of the world. *Int Geol Rev*. 2002;44:1092–1104.
2. Wilhelm DJ, Simbeck DR, Karp AD, Dickenson RL. Syngas production for gas-to-liquids applications: technologies, issues and outlook. *Fuel Process Technol*. 2001;71:139–148.
3. Freni S, Calogero G, and Cavallaro S. Hydrogen production from methane through catalytic partial oxidation reactions. *J Power Sources*. 2000;87:28–38.
4. Schmidt LD, Siddall J, Bearden M. New ways to make old chemicals. *AIChE J*. 2000;46:1492–1495.
5. Fleisch TH, Sills RA, Briscoe MD. 2002—Emergence of the gas-to-liquids industry: a review of global GTL developments. *J Nat Gas Chem*. 2002;11:1–14.
6. Lange JP, Schoonebeek RJ, Mercera PDL, van Breukelen FW. Oxycracking of hydrocarbons: chemistry, technology and economic potential. *Appl Catal A: Gen*. 2005;283:243–253.
7. York APE, Xiao T, Green MLH. Brief overview of the partial oxidation of methane to synthesis gas. *Top Catal*. 2003;22:345–358.
8. Horn R, Williams KA, Degenstein NJ, Schmidt LD. Syngas by catalytic partial oxidation of methane on rhodium: mechanistic conclusions from spatially resolved measurements and numerical simulations. *J Catal*. 2006;242:92–102.
9. Hickman DA, Schmidt LD. Steps in CH_4 oxidation on Pt and Rh surfaces: high-temperature reactor simulations. *AIChE J*. 1993;39:1164–1177.
10. Deutschmann O, Schmidt LD. Modeling the partial oxidation of methane in a short-contact-time reactor. *AIChE J*. 1998;44:2465–2477.
11. Goralski CT, O'Connor RP, Schmidt LD. Modeling homogeneous and heterogeneous chemistry in the production of syngas from methane. *Chem Eng Sci*. 2000;55:1357–1370.
12. Deutschmann O, Schwiedernoch R, Maier LI, Chatterjee D. Natural gas conversion in monolithic catalysts: interaction of chemical reactions and transport phenomena. *Stud Surf Sci Catal*. 2001;136:251–258.
13. Schwiedernoch R, Tischer S, Correa C, Deutschmann O. Experimental and numerical study on the transient behavior of partial oxidation of methane in a catalytic monolith. *Chem Eng Sci*. 2003;58:633–642.
14. Huff MC, Androulakis IP, Sinfelt JH, Reyes SC. The contribution of gas-phase reactions in the Pt-catalyzed conversion of ethane-oxygen mixtures. *J Catal*. 2000;191:46–54.
15. Zerkle DK, Allendorf MD, Wolf M, Deutschmann O. Understanding homogeneous and heterogeneous contributions to the platinum-catalyzed partial oxidation of ethane in a short-contact-time reactor. *J Catal*. 2000;196:18–39.
16. Donsì F, Williams KA, Schmidt LD. A multistep surface mechanism for ethane oxidative dehydrogenation on Pt- and Pt/Sn-coated monoliths. *Ind Eng Res Chem*. 2005;44:3453–3470.
17. Hickman DA, Schmidt LD. Production of syngas by direct catalytic oxidation of methane. *Science*. 1993;259:343–346.
18. Marinov NM, Pitz WJ, Westbrook CK, Vincitore AM, Castaldi MJ, Senkan SM, Melius CF. Aromatic and polycyclic aromatic hydrocarbon formation in a laminar premixed *n*-butane flame. *Combust Flame*. 1998;114:192–213.
19. Smith GP, Golden DM, Frenklach M, Moriarty NW, Eiteneer B, Goldenberg M, Bowman CT, Hanson RK, Song S, Gardiner WC Jr., Lissianski VV, Qin Z. GRI Mechanism, Version 3.0. Available at http://www.me.berkeley.edu/gri_mech/. Access date, March 2004.
20. Veser G, Frauhammer J. Modeling steady state and ignition during catalytic methane oxidation in a monolith reactor. *Chem Eng Sci*. 2000;55:2271–2286.
21. Slaa JC, Berger RJ, Marin GB. Partial oxidation of methane to synthesis gas over Rh/α-Al_2O_3 at high temperatures. *Catal Lett*. 1997;43:63–70.
22. Tummala S. *Staged Catalysts for Millisecond Contact Time Reactions*, PhD Thesis. University of Minnesota: Minnesota, 2000.
23. Klein EJ, Tummala S, Schmidt LD. Catalytic partial oxidation of methane to syngas: staged and stratified reactors with steam addition. *Stud Surf Sci Catal*. 2001;136:245–250.
24. Wei J, Iglesia E. Isotopic and kinetic assessment of the mechanism of reactions of CH_4 with CO_2 or H_2O to form synthesis gas and carbon on nickel catalysts. *J Catal*. 2004;224:370–383.
25. Bizzi M, Saracco G, Schwiedernoch R, Deutschmann O. Modeling the partial oxidation of methane in a fixed bed with detailed chemistry. *AIChE J*. 2004;50:1289–1299.
26. Williams KA, Leclerc CA, Schmidt LD. Rapid lightoff of syngas production from methane: a transient product analysis. *AIChE J*. 2005;51:247–260.
27. Mhadeshwar AB, Vlachos DG. Hierarchical multiscale mechanism development for methane partial oxidation and reforming and for thermal decomposition of oxygenates on Rh. *J Phys Chem B*. 2005;109:16819–16835.

28. Horn R, Degenstein NJ, Williams KA, Schmidt LD. Spatial and temporal profiles in millisecond partial oxidation processes. *Catal Lett*. 2006;110:168–179.
29. Basile F, Fornasari G, Trifiro F, Vaccari A. Partial oxidation of methane. Effect of reaction parameters and catalyst composition on the thermal profile and heat distribution. *Catal Today*. 2001;64:21–30.
30. Basini L, Aasberg-Petersen K, Guarinoni A, Ostberg M. Catalytic partial oxidation of natural gas at elevated pressure and low residence time. *Catal Today*. 2001;64:9–20.
31. Bizzi M, Basini L, Saracco G, Specchia V. Short contact time catalytic partial oxidation of methane: analysis of transport phenomena effects. *Chem Eng J*. 2002;90:97–106.
32. Marengo S, Comotti P, Galli G. New insight into the role of gas phase reactions in the partial oxidation of butane. *Catal Today*. 2003;81:205–213.
33. Li B, Maruyama K, Nurunnabi M, Kunimori K, Tomishige K. Temperature profiles of alumina-supported noble metal catalysts in autothermal reforming of methane. *Appl Catal A: Gen*. 2004;275: 157–172.
34. Henning DA, Schmidt LD. Oxidative dehydrogenation of ethane at short contact times: species and temperature profiles within and after the catalyst. *Chem Eng Sci*. 2002;57:2615–2625.
35. Bond TC, Noguchi RA, Chou C-P, Mongia RK, Chen J-Y, Dibble RW. Catalytic oxidation of natural gas over supported platinum: flow reaction experiments and detailed numerical modeling. In: *Proceedings of the 26th International Symposium on Combustion*, Vol. 1. Combustion Institute, Pittsburgh, PA. 1996;1771–1778.
36. Lyubovsky M, Roychoudhury S, LaPierre R. Catalytic partial "oxidation of methane to syngas" at elevated pressures. *Catal Lett*. 2005;99:113–117.
37. Sidwell RW, Zhu H, Kee RJ, Wickham DT. Catalytic combustion of premixed methane-in-air on a high-temperature hexaaluminate stagnation surface. *Combust Flame*. 2003;134:55–66.
38. Sidwell RW, Zhu H, Kibler BA, Kee RJ, Wickham DT. Experimental investigation of the activity and thermal stability of hexaaluminate catalysts for lean methane-air combustion. *Appl Catal A: Gen*. 2003;255:279–288.
39. Reinke M, Mantzaras J, Schaeren R, Bombach R, Inauen A, Schenker S. High-pressure catalytic combustion of methane over platinum: in situ experiments and detailed numerical predictions. *Combust Flame*. 2004;136:217–240.
40. Reinke M, Mantzaras J, Bombach R, Schenker S, Inauen A. Gas phase chemistry in catalytic combustion of methane/air mixtures over platinum at pressures of 1 to 16 bar. *Combust Flame*. 2005; 141:448–468.
41. Grunwaldt JD, Baiker A. Axial variation of the oxidation state of Pt-Rh/Al_2O_3 during partial methane oxidation in a fixed-bed reactor: an in situ X-ray absorption spectroscopy study. *Catal Lett*. 2005;99:5–12.
42. Grunwaldt J-D, Hannemann S, Schroer CG, Baiker A. 2D-mapping of the catalyst structure inside a catalytic microreactor at work: partial oxidation of methane over Rh/Al_2O_3. *J Phys Chemstry B*. 2006;110:8674–8680.
43. Horn R, Williams KA, Degenstein NJ, Schmidt LD. Mechanism of H2 and CO formation in the catalytic partial oxidation of CH4 on Rh probed by steady-state spatial profiles and spatially resolved transients. *Chem Eng Sci*. 2007;62:1298–1307.
44. Coltrin ME, Kee RJ, Rupley FM, Meeks E. *Surface chemkin III: A Fortran package for the analyzing heterogeneous chemical kinetics at a solid-surface – gas-phase interface*. Technical Report SAND96-8217, Sandia National Laboratories, 1996.
45. Kee RJ, Rupley FM, Miller JA, Coltrin ME, Grcar JF, Meeks E, Moffat HK, Lutz AE, Dixon-Lewis G, Smooke MD, Warnatz J, Evans GH, Larson RS, Mitchell RE, Petzold LR, Reynolds WC, Caracotsios M, Stewart WE, Glarborg P. PLUG: A program for the analysis of plug-flow reactors with gas-phase and surface chemistry. In: *CHEMKIN Collection, Release 3.5*. San Diego, CA: Reaction Design, 1999.
46. Deutschmann O, Tischer S, Correa C, Chatterjee D, Kleditzsch S, Janardhanan VM. *DETCHEM Software Package* (*2.0 edition*). Karlsruhe, Germany, 2005.
47. Incropera FP, DeWitt DP. *Fundamentals of Heat and Mass Transfer*, *4th ed*. New York: Wiley, 1996.
48. General Electric. Quartz: thermal conductivity chart created with manufacturer's data. Available at http://www.gequartz.com/en/thermal.htm. Accessed March 2004.
49. Mazumder S, Sengupta D. Sub-grid scale modeling of heterogeneous chemical reactions and transport in full-scale catalytic converters. *Combust Flame*. 2002;131:85–97.
50. Fluent. *Fluent 6.2 Computational Fluid Dynamics Software User's Guide*. Fluent: Lebanon, NH, 2005.
51. Twigg MV, Richardson JT. Theory and applications of ceramic foam catalysts. *Chem Eng Res Des*. 2002;80:183–189.
52. Richardson JT, Peng Y, Remue D. Properties of ceramic foam catalyst supports: pressure drop. *Appl Catal A: Gen*. 2000;204:19–32.
53. Moreira EA, Coury JR. The influence of structural parameters on the permeability of ceramic foams. *Braz J Chem Eng*. 2004;21:23–33.
54. Zhao CY, Lu TJ, Hodson HP, Jackson JD. The temperature dependence of effective thermal conductivity of open-celled steel alloy foams. *Mater Sci Eng A: Struct Mater Properties, Microstruct Process*. 2004;A367:123–131.
55. Hohn KL, Schmidt LD. Partial oxidation of methane to syngas at high space velocities over Rh-coated spheres. *Appl Catal A: Gen*. 2001;211:53–68.
56. Sweeting TB, Norris DA, Strom LA, Morris JR. Reticulated ceramics for catalyst support applications. *Mater Res Soc Symp Proc*. 1995;368:309–314.
57. Wolf D, Hoehenberger M, Baerns M. External mass and heat transfer limitations of the partial oxidation of methane over a Pt/MgO catalyst-Consequences for adiabatic reactor operation. *Ind Eng Chem Res*. 1997;36:3345–3353.
58. Schneider A, Mantzaras J, Jansohn P. Experimental and numerical investigation of the catalytic partial oxidation of CH_4/O_2 mixtures diluted with H_2O and CO_2 in a short contact time reactor. *Chem Eng Sci*. 2006;61:4634–4649.
59. Coltrin ME, Moffat HK, Kee RJ, Rupley FM. *CRESLAF, Version 4.0: A Fortran Program for Modeling Laminar, Chemically Reacting, Boundary-Layer Flow in Cylindrical or Planar Channels*. San Diego, CA: Reaction Design, 1993.
60. Jacobs LLG, Lednor PW, Limahelu AGG, Schoonebeek RJ, Vonkeman KA (to Shell Oil Company). Process for the catalytic partial oxidation of hydrocarbons. US patent 5,510,056. 1996.
61. Degenstein NJ, Subramanian R, Schmidt LD. Partial oxidation of *n*-hexadecane at short contact times: catalyst and washcoat loading and catalyst morphology. *Appl Catal A: Gen*. 2006;305:146–159.
62. Raja LL, Kee RJ, Deutschmann O, Warnatz J, Schmidt LD. A critical evaluation of Navier-Stokes, boundary-layer, and plug-flow models of the flow and chemistry in a catalytic-combustion monolith. *Catal Today*. 2000;59:47–60.
63. Stutz MJ and Poulikakos D. Effects of microreactor wall heat conduction on the reforming process of methane. *Chem Eng Sci*. 2005;60:6983–6997.

Manuscript received Oct. 26, 2006, and revision received May 23, 2007.